

Microscopic origin of charge impurity scattering and flicker noise in MoS₂ field effect transistors

Subhamoy Ghatak¹, Sumanta Mukherjee², Manish

Jain¹, D. D. Sarma² and Arindam Ghosh¹

¹*Department of Physics, Indian Institute of Science, Bangalore 560 012, India and*

²*Solid State Structural Chemistry Unit,*

Indian Institute of Science, Bangalore 560 012, India

Abstract

Scattering of charge carriers and flicker noise in electrical transport are the central performance limiting factors in electronic devices, but their microscopic origin in molybdenum disulfide (MoS₂)-based field effect transistors remains poorly understood. Here, we show that both carrier scattering and low-frequency $1/f$ noise in mechanically exfoliated ultra-thin MoS₂ layers are determined by the localized trap states located within the MoS₂ channel itself. The trap states not only act as Coulomb scattering centers that determine transport in both equilibrium ($eV < k_B T$) and non-equilibrium ($eV > k_B T$) regimes, where V and T are the source drain bias and temperature respectively, but also exchange carriers with the channel to produce the conductivity noise. The internal origin of the trap states was further confirmed by studying noise in MoS₂ films deposited on crystalline boron nitride substrates. Possible origin and nature of the trap states is also discussed.

Atomically thin films of MoS₂ have emerged as a promising platform for transparent flexible electronics. In the field effect geometry, MoS₂ offers several advantages that include large on-off ratio, immunity against short channel effects, and small subthreshold swing^{1,2}. These promise MoS₂-based logic devices^{3,4} and energy-efficient field effect transistor⁵⁻⁷, but in the generic back gated geometry, the electron mobility of MoS₂ field effect devices (MoS₂ FET) is generally poor ($\lesssim 20 \text{ cm}^2/\text{Vs}$), which may restrict its application as fast transistors and rf devices⁸. Since the phonon-limited room temperature mobility⁹ in MoS₂ can be as large as $\sim 400 \text{ cm}^2/\text{V.s}$, the factors that restrict carrier mobility in MoS₂ are of great research interest¹⁰. Recently, some studies have reported to achieve higher mobility in top gated devices with a high- k dielectric^{1,11,12}. This suggest that charged defects play a crucial role in determining the performance of MoS₂-based transistors, but the microscopic origin of these defects has remained unclear.

Disorder in ultra-thin MoS₂ transistor may arise due to both external and internal factors. The former, which primarily involves substrate-bound charge traps, roughness or adsorbates, was shown to affect both electron mobility and flicker noise in graphene FETs¹³⁻¹⁶. Although a similar picture has been suggested for MoS₂ as well^{12,17,18}, the occurrence of strong localization even near room temperature and at high carrier density indicate a much stronger disorder in MoS₂. Among the internal factors, sulphur vacancies are often discussed which can introduce localized donor states inside the bandgap and determine the electrical transport properties¹⁹. It has been reported that presence of atmospheric oxygen and water vapour can lead to oxidation of MoS₂ resulting in MoO₃²⁰. Moreover, nucleation of metallic 1T polytrope and the grain boundaries can also act as structural disorder as observed in chemically exfoliated MoS₂²¹.

To address the origin of performance-limiting disorder, we have carried out electrical transport measurements combined with time dependent conductance fluctuations *i.e.* $1/f$ noise. The purpose of employing $1/f$ noise stems from its sensitivity to both structural inhomogeneity in solids,²² and charge traps in proximity to the channel as shown for graphene^{16,23,24} and silicon FETs^{25,26}. In our experiments, carrier density dependence of both conductivity and noise measurements suggest that disorder is dominated by trapped charges. However, the trap density calculated from both turned out two orders of magnitude higher than the SiO₂ surface trap density, suggesting that the traps are internal to bulk of MoS₂ films. This observation was also supported by $1/f$ noise measurement in MoS₂ devices

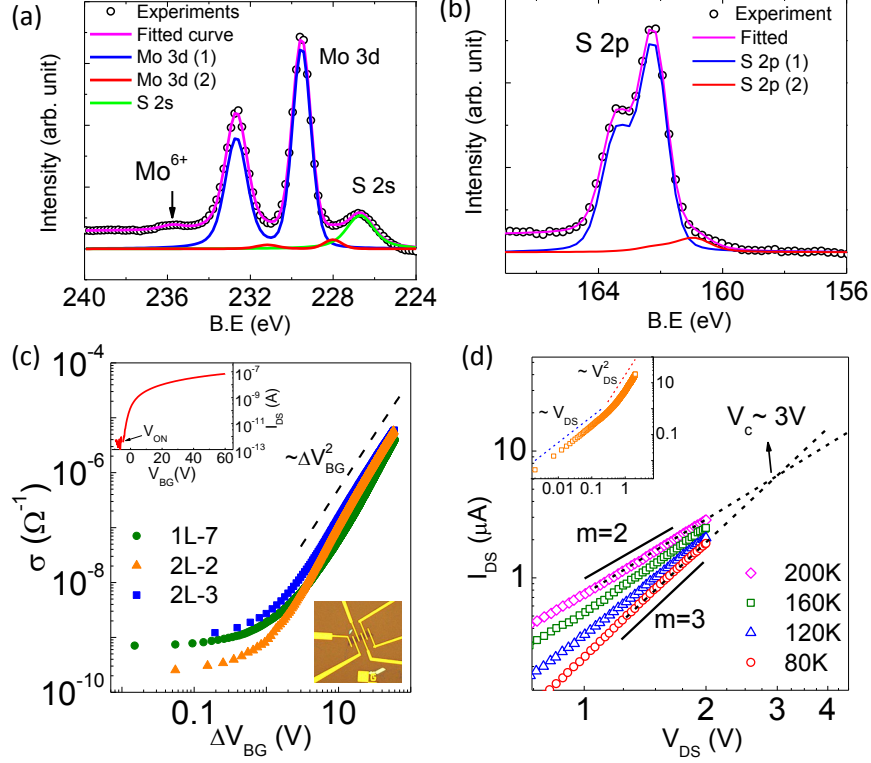


FIG. 1: (a) Deconvolution of the experimental photo electron spectra (black open circles) of Mo 3d to obtain different crystallographic components namely 2H phase (blue line). The red line indicates presence of additional phase (see text). The solid orange line is the overall simulated spectra. (b) Similar deconvolution of S 2p spectra. (c) Conductivity showing a ΔV_{BG}^2 dependence at high T and V_{BG} for three different devices. Inset: Transfer characteristics of a single layer MoS₂ device on SiO₂ substrate with $V_{DS} = 10$ mV (top-left), and Optical micrograph of a single layer MoS₂ device on Si/SiO₂ wafer with 300 nm oxide. The scale bar is 10 μm (bottom-right). (d) $I_{DS} - V_{DS}$ measurement of the 1L-8 device at high V_{DS} and $T < 200$ K. Inset: Ohmic and non-Ohmic regions of the $I_{DS} - V_{DS}$ characteristic at 300 K.

on trap-free hexagonal boron nitride (hBN) substrate.

Bulk MoS₂ crystals were obtained from SPI supplies and were at first thoroughly characterized with X-ray photoemission spectroscopy (XPS) and Raman spectroscopy (See Fig. S1e in supplementary material). Mo 3d and S 2p XPS spectra obtained from the bulk crystal are shown as open circles in Fig. 1a and 1b along with various component spectra obtained from spectral decomposition. The major contribution in both Mo 3d and S 2p peaks arises due

to 2H phase (blue lines) of MoS_2 ²¹, although additional features (red lines) at lower binding energies were observed in both spectra at 4% intensity ratio (see supplementary material for details). This suggests presence of structural inhomogeneity in bulk MoS_2 crystals. For electrical characterization, single and bilayer MoS_2 flakes were exfoliated from bulk crystals on 300 nm Si/SiO₂ wafer using the scotch tape technique. Contact pads were designed using standard ebeam lithography and metallization (see experimental details in supplementary material). An optical micrograph of a typical device is shown in bottom-right inset of Fig. 1c. Two-probe conductance measurement was adapted due to high resistance of the samples. In all devices (see TABLE I in supplementary material), the current-voltage ($I_{DS} - V_{DS}$) characteristics were linear around room temperature at high back gate voltage (V_{BG}) and low source-drain bias $V_{DS} \leq 100$ mV (see Fig. S5 in supplementary material). The characteristics became slowly non-linear as temperature was decreased. Both conductivity(σ) and $1/f$ -noise in current were measured in the linear current-voltage regime. This restricted the excitation bias to $V_{DS} \leq 10$ mV. Although in 2-probe measurement contact resistance can not be avoided, our devices shows much higher total resistance than typical contact resistance (R_c), reported recently by Transmission Line Measurement (TLM) study for Au contacted MoS_2 devices with similar transfer characteristics².

The backgate transfer characteristics of a typical single layer device at 300 K is shown in top-left inset of Fig. 1c. The conduction occurred at positive V_{BG} indicating an intrinsic n -doping of the channel. We defined V_{ON} (top-left inset of Fig. 1c) as the backgate voltage at which the current through the device became measurable ($> 10^{-12}$ A) at $T = 300$ K. The parameter $\Delta V_{BG} = V_{BG} - V_{ON}$, is then approximately proportional to carrier density (n) particularly at high ΔV_{BG} . In Fig. 1c, we have plotted conductivity as function of ΔV_{BG} for three different devices and found $\sigma \propto \Delta V_{BG}^2$ for $\Delta V_{BG} \geq 6$ V. This indicates that the charge transport is dominated by unscreened Coulomb impurity scattering²⁷. Such ΔV_{BG}^2 dependence was observed in *all* the devices around 300 K.

To explore the microscopic origin of the charged impurities or traps, we perform $I_{DS} - V_{DS}$ measurements at high source-drain bias, which is a sensitive tool to investigate the disorder configuration in organic thin film transistors^{28,29} and reduced graphene oxide³⁰. At low source-drain bias $I_{DS} \propto V_{DS}$, although it deviated from linearity as V_{DS} was increased leading to $I_{DS} \propto V_{DS}^m$ with $m \geq 2$ particularly below 200 K (inset of Fig. 1d). The $I_{DS} - V_{DS}$ characteristics in our devices were highly symmetric in the entire drain-source

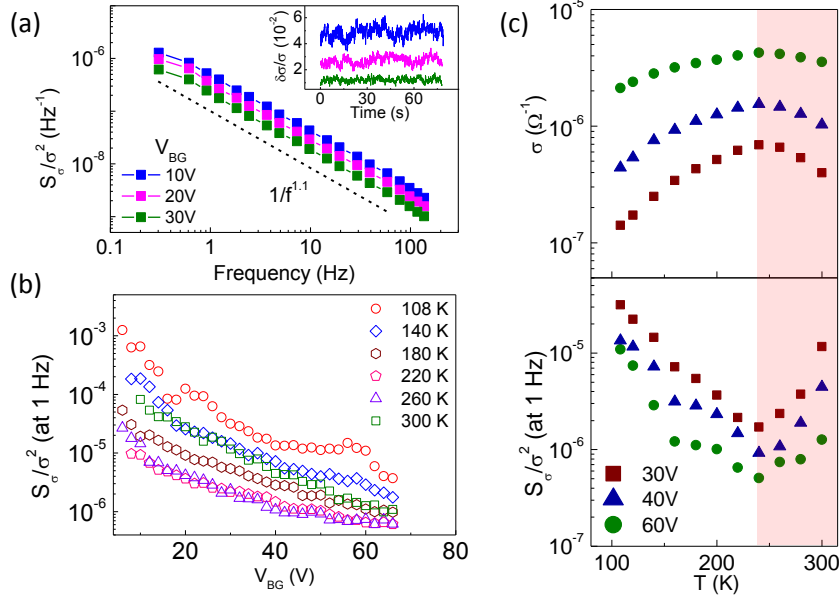


FIG. 2: (a) $1/f$ noise power spectrum of conductivity fluctuations at three different V_{BG} . The inset shows corresponding conductivity fluctuations as a function of time at the same gate voltages. (b) Gate voltage dependence of noise power spectral density S_σ/σ^2 at various T for a single layer device. (c) Non-monotonic T dependence of both σ and S_σ/σ^2 for 1L-2 device at three different V_{BG} . The localized regime was observed below 240 K (unshaded) and the weak metallic regime for $T > 240$ K (shaded).

voltage range which eliminates dominance of Schottky barrier at the contact (see Fig. S5 in supplementary material). Therefore, we attribute this to trap-assisted space charge limited conduction (SCLC) in MoS₂ devices and hence presence of an exponential distribution of trap states³¹. An exponential distribution can not originate from SiO₂, indicating a bulk or structural origin of these trap states which also leads to charged impurity scattering when occupied. In SCLC regime, the critical voltage (V_c) where $I_{DS} - V_{DS}$ curves at different temperature intersect each other³² (Fig. 1d) provides an estimation of volume trap density N_T . N_T is related to V_c by the relation $N_T = 2\epsilon_r\epsilon_0 V_c/qL^2$. We obtained $V_c \approx 3$ V by extrapolating the $I_{DS} - V_{DS}$ characteristics and found $N_T \sim 2 \times 10^{17}$ cm⁻³ for 1L-8 device, where $\epsilon_r \approx 3.3$ is the relative permittivity of MoS₂.

We now focus on the low-frequency conductivity fluctuations (inset of Fig. 2a) in our MoS₂ devices. The normalized power spectral densities (S_σ/σ^2) of conductivity fluctuations showed $1/f$ -type frequency spectrum at low frequencies (Fig. 2a). The gate voltage

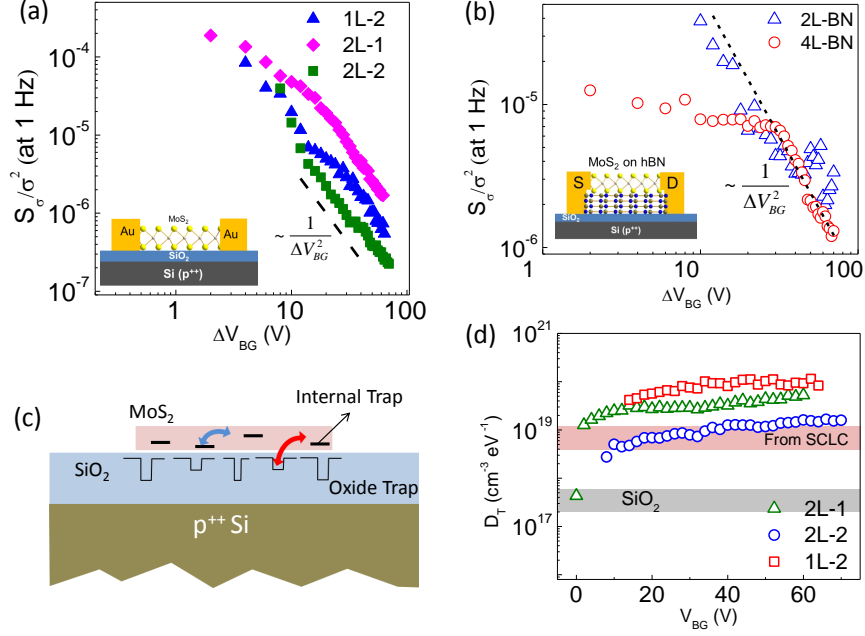


FIG. 3: (a) $1/\Delta V_{BG}^2$ dependence of S_σ/σ^2 at high V_{BG} and near room temperature for three different MoS₂ devices on SiO₂ substrate. The schematic of an ‘MoS₂ on SiO₂’ device is shown in the inset. (b) Similar noise behaviour in ‘MoS₂ on hBN’ devices. The inset shows the schematic of a MoS₂ device on hBN substrate. (c) Trap states in MoS₂ transistor can arise either due to external oxide traps or internal structural disorders. (d) Experimentally calculated trap density D_T as a function of V_{BG} for three different devices. The same for standard SiO₂ substrate (grey band) and from SCLC (red band).

dependence of S_σ/σ^2 is shown in Fig. 2b. We observed that S_σ/σ^2 decreases monotonically with increasing gate voltage at a fixed temperature. The temperature dependence of both σ and S_σ/σ^2 at three fixed V_{BG} are shown in Fig. 2c. We observed that both change non-monotonically. The sharp decrease in σ below 240 K can be readily attributed to the localized state transport¹⁸, where S_σ/σ^2 increases exponentially due to the broad distribution of the waiting time of the carriers between successive hops³³. However, for $T > 240$ K and especially at large V_{BG} , where σ displays a metal-like transport^{34,35}, the noise magnitude increases with increasing temperature as in a diffusive quasi-metallic systems³⁶. It should be mentioned here that such weak diffusive transition was not observed in some devices till 300 K (see supplementary material for more discussions).

The carrier density dependence of S_σ/σ^2 for three different devices is shown in Fig. 3a.

We observe that at low ΔV_{BG} , the variation differs from one sample to another and may be connected to the details of electron localization. However, at large ΔV_{BG} , *all* devices show $S_\sigma/\sigma^2 \propto 1/\Delta V_{BG}^2$, which is a characteristic feature of *number fluctuation* in semiconductors³⁷. Number fluctuation arises from trap states varying in energy and position within or close to the conduction channel (see schematic in Fig. 3c). The interfacial trap states in the SiO₂ substrate close to channel has been quantitatively shown to cause similar scenario in graphene-on-SiO₂^{16,24,38} and Si-MOSFETs²⁵. To check whether the oxide traps can account for the observed noise, we calculate the oxide trap density D_T per unit volume and energy using the trap-channel tunnel model, developed originally for MOSFETs^{25,26}. The calculated D_T has been plotted in Fig. 3d for three different devices which is approximately two orders of magnitude higher than SiO₂ surface trap density (see supplementary for detail calculations). To find an alternative source, we calculate the trap density of states from its volume density N_T obtained from the SCLC measurements (Fig. 2d). Assuming $N_T \approx 1 - 3 \times 10^{17} \text{ cm}^{-3}$ as estimated from SCLC, and the trap states in an energy bandwidth of $k_B T \sim 26 \text{ meV}$ contribute to carrier number fluctuation, we calculate trap state density $D_T = N_T/26(\text{meV}) \approx 4 \times 10^{18} - 10^{19} \text{ cm}^{-3}\text{eV}^{-1}$ which reasonably agrees with the values calculated using number fluctuation model for devices 2L-1 and 2L-2 (see Fig. 3d). The higher value D_T for 1L-2 device can be attributed to the error introduced during the calculation of transconductance g_m due to contact resistance (see supplementary material). A recent study has shown a similar order of trap density in MoS₂ thin film transistors³⁹. This establishes that a set of structurally originated Coulomb scatterer determine both electrical transport and low frequency noise in MoS₂ transistors whereas the interfacial oxide trap charges plays a minimal role in the transport properties.

We further confirm this result by fabricating MoS₂ transistor on crystalline hexagonal boron nitride (hBN) substrate known to be free from surface trap states and dangling bonds⁴⁰ (see inset of Fig. 3b and detail in supplementary). This device architecture eliminates the oxide trap states to cause carrier exchange with the channel. Noise measurements on two ‘MoS₂ on hBN’ devices are shown in Fig. 3b. We find that $S_\sigma/\sigma^2 \propto 1/\Delta V_{BG}^2$ at large ΔV_{BG} which establishes number fluctuation as the dominant noise mechanism providing further support to the internal origin of the localized trap states.

It is well-known that the presence of water vapour and fabrication-induced resist residues can also act as an additional source of trap states in thin film transistors. In order to

address the contribution of these external sources, we also fabricate devices by transferring a thin (20 nm) single crystalline layer of hBN on top of the MoS₂ flake prior to lithography processes (see insets of Fig. 4b and 4d for schematic and actual device images respectively). This protects the channel from acrylic residues and the possibility of presence of water vapour is also minimal as the transfer was done at 100⁰C. The measurements were performed before and after vacuum annealing at 150⁰C and 4.6×10⁻⁶ mbar vacuum for 3 hours. We found that in all cases the V_{ON} shifted towards large (< -60 V) negative gate voltages after annealing. This has been observed previously but the reason behind this remained controversial³⁵. The transfer characteristics for both kinds of devices are plotted in Fig. 4a and 4b respectively as a function of ΔV_{BG} . We find that the characteristics curves show similar density dependence beyond $\Delta V_{BG} > 10$ V indicating a minimal role of the contacts in these devices. The noise behaviour is shown in this regime for both kind of devices before and after annealing in Fig. 4c and 4d respectively. For comparison, we define plot S_I/I^2 normalized to its magnitude at $\Delta V_{BG} \approx 10$ V. We find that, in spite of having similar transfer characteristics, the noise magnitude decreases by 10 - 30 times on annealing irrespective of the nature of surface protection. This observation suggests that in our devices where the measurements are carried out in high vacuum condition, the noise is not dominated by the external sources of trap states.

The noise measurement in conjunction with the low temperature conductivity measurement can provide a crucial insight on the structural morphology of the trap states. We observed that, at low temperature, conductivity as a function of gate voltage showed a number of reproducible peaks even at high carrier density ($V_{BG} \sim 60 - 80$ V and see Fig. S7 in supplementary material and ref.¹⁸). This indicates strong charge inhomogeneity in the MoS₂ channel. Oscillatory conductivity also suggests that the charge inhomogeneous regions (patches) act like quantum dots in semiconducting MoS₂ channel. These patches can exchange electrons with the channel to produce $1/f$ noise (Fig. 5a), and also act as charged impurities. For a more quantitative approach, we consider D and $\Delta E = e^2/C$ (where $C \approx 4\epsilon_0\epsilon_r D$ is the capacitance) as the average diameter and charging energy respectively of the patches. Because of their small size ($D \sim 10$ nm)¹⁸, we also considered single particle quantum level spacing as ΔE_Q . The scenario has been depicted in the schematic of Fig. 5a (bottom). Assuming that the channel is nearly diffusive at high T and noise arises due to thermally activated exchange of charge carriers between channel and patches, the

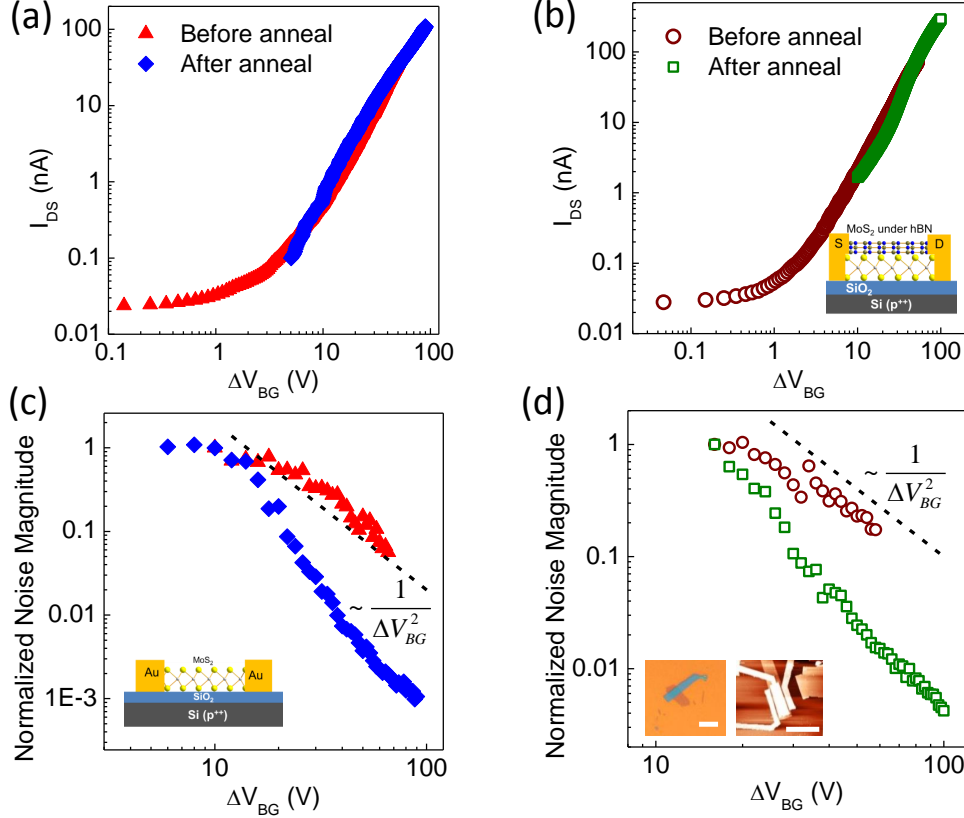


FIG. 4: (a),(b) Transfer characteristics before and after annealing of MoS₂ channel with open and protected upper surface. The inset in 4b shows schematic of an hBN protected MoS₂ device. (c),(d) Noise behaviour in the same devices before and after annealing. S_I/I^2 was normalized with its values at $\Delta V_{BG} = 10$ V and 16 V in Fig. 4c and 4d respectively. The black dashed lines indicate $1/\Delta V_{BG}^2$. The inset in figure 4d show an optical micrograph of hBN flake on single layer MoS₂ flake and atomic force microscopy image of final device. Both the scale bars are 8 μ m.

noise magnitude can be expressed as (see full derivation in the supplementary material):

$$\frac{\langle \delta \sigma^2 \rangle}{\sigma^2} \approx \left[\frac{k_B T}{\Delta E_Q} \right]^3 \frac{N_E}{N^2} \exp \left[-\frac{\Delta E}{k_B T} \right] \quad (1)$$

where N_E and N are the total number of patches and total number of electrons respectively in the channel. Equation 1 suggests an exponential temperature dependence in diffusive regime (shaded region in Fig. 2c). To verify this, we chose the devices which showed an insulator to weak diffusive transition^{34,35} at high T . The variation of $T^{-3} \langle \delta \sigma^2 \rangle / \sigma^2$ as a function of $1/T$ (see Fig. 5b) in the high T region yields average charging energy $\Delta E \sim 88 \pm 15$ meV

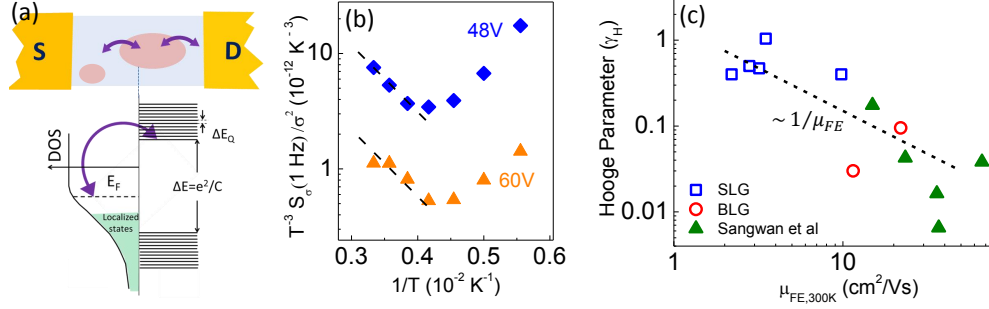


FIG. 5: (a) Scematic representation of charge exchange between Coulomb blockaded localized state and semiconducting channel (up). The same in the energy diagram (down). (b) $T^{-3}S_\sigma/\sigma^2$ as function of $1/T$ for 1L-2 device at $V_{BG} = 48, 60 \text{ V}$. The slope of the exponential fit gives the charging energy ΔE . (c) Hooge parameter (γ_H) as a function of field effect mobility (μ_{FE}) for five single layer (blue square) and two bilayer (red circle) devices at $\Delta V_{BG} \sim 58 \text{ V}$ and 300 K. The filled triangles indicate the γ_H calculated in ref [42] in similar MoS₂ devices. The dotted line represents variation of γ_H inversely proportional to μ_{FE} .

for the device 1L-1. A similar calculation of ΔE for device 1L-2, which also showed a weak diffusive transition, gives charging energy of $90 \pm 20 \text{ meV}$ (see supplementary Fig. S8). It should be noted that charge exchange can last well upto the room temperature and beyond due to large charging energy. We use the Hooge relation $S_\sigma/\sigma^2 = \gamma_H/nAf$ to compare the noise magnitude from different devices, where γ_H , A and n are the Hooge parameter, area of the channel, and electron density calculated from ΔV_{BG} using the capacitance between the channel and the backgate (The Hooge relation is not strictly valid in the McWhorter-type number fluctuation noise, and should be taken only as a guideline). Since $\sigma \propto n^2$ (Fig. 1a) in the diffusive regime, $\gamma_H \propto 1/\mu_{FE}$ (derivation in supplementary material and also see Ref[41]), which provides a reasonable description of the noise measured in this work (calculated at $\Delta V_{BG} \approx 58 \text{ V}$, and $f = 1 \text{ Hz}$), as well as that in Ref[42] (see Fig. 5c). We observe that the noise level is much higher in MoS₂ films compared to graphene device at similar carrier densities and on same substrate. This also strengthens our conclusion of an internal origin of disorder in MoS₂ films.

We now discuss the possible origin of these charge inhomogeneous patches in MoS₂ films. Recently, it has been reported that both n -type and p -type charge inhomogeneity can occur in natural MoS₂ crystal, and are related to the crystal structure⁴³. The low sulphur

concentration regions (S-vacancies or Mo-like cluster) act as nanometer sized metallic regions and can take part in electron exchange. Such sulphur deficit region in our devices can originate either during crystal growth or during mechanical exfoliation. Moreover, *p*-type regions are formed due to structural defects to reduce strain in sulphur rich areas. We also discuss one more possibility which was revealed from our XPS measurement where it was observed that the positions of the extra peaks match well with the metastable 1T phase of MoS₂²¹. The 1T phase, which may nucleate around sulphur vacancies or other crystalline disorder, is metallic in nature, and can introduce charge inhomogeneity in semiconducting 2H-MoS₂. The strong suppression in noise after annealing in both surface-protected and unprotected devices provides additional support towards such bulk inhomogeneity-driven noise mechanism in MoS₂ FETs. Annealing can not only modify the layout of individual defect or cluster, but also decrease the 1T fraction significantly²¹. Finally, for a quantitative estimate, we calculate the number of charge inhomogeneous patches per unit volume $N_p \sim 0.05/D^2t \approx 2 \times 10^{17} \text{cm}^{-3}$, where we take $D \sim 15 \text{ nm}$, and $t \sim 1 \text{ nm}$ as the thickness of MoS₂ layer. This value agrees closely with the N_T value calculated from SCLC measurement. Moreover, we calculate $N_E = N_p \times At$, where A is the area of the channel. Using equation 1 and some typical values of the parameters obtained from experiment, we obtain $\gamma_H \approx 0.2$ at $n = 4.5 \times 10^{12} \text{ cm}^{-2}$ (see supplementary for calculation and equation S15). This value agrees reasonably with the γ_H values obtained directly from the experiment (See Fig. 4c).

In conclusion, we have studied electrical conductivity and low frequency noise in ultrathin MoS₂ transistor. We found that both are dominated by same set of localized trap states. The trap density was calculated independently from both non-equilibrium conductivity and noise measurements which agree well and turn out much higher than SiO₂ surface trap density. This strongly suggests that the trap states are not external, but related to the crystal structure of the MoS₂ film that determines electron transport in MoS₂ field effect transistors.

Supplementary information

Microscopic origin of charge impurity scattering and flicker noise in MoS₂ field effect transistors

A. Experimental details:

For ‘MoS₂ on SiO₂’ devices, MoS₂ flakes were exfoliated on SiO₂ (300 nm)/n⁺⁺ Si wafer from bulk MoS₂ crystals (SPI Supplies) using scotch tape. To keep the disorder level comparable, the wafers were thoroughly cleaned by standard RCA cleaning followed by acetone and isopropyl alcohol cleaning in ultrasonic bath. The flakes were identified initially by optical microscope^{44,45}. The thickness and quality of each flake was determined by Raman spectroscopic measurement⁴⁶(see Figure S1). The Raman data was recorded using WITEC confocal (X100 objective) spectrometer with 600 lines/mm grating, 514.5 nm excitation at a very low laser power level (less than 1 mW) to avoid any heating effect. Au(40 nm) contacts were defined using standard electron beam lithography followed by thermal evaporation of 40 nm Au and lift-off in hot acetone. No Ar/H₂ annealing was done in any of our devices after liftoff because we found change in morphology of only Au (no underlayer like Ti or Cr) pads on SiO₂ substrate after annealing beyond 250°C.

To transfer MoS₂ on hexagonal boron nitride (hBN: from Momenitive), we prepared two different substrates⁴⁷. First, 10-20 nm hBN on Si/SiO₂ wafer and a glass slide coated with transparent tape and 400 nm thick EL9 (Microchem). MoS₂ flakes were exfoliated using scotch tape technique on the glass-tape-EL9 stack. The transfer was done in MJB3 Mask aligner with a heated stage at 100°C to reduce the water vapour at the interface (see Fig. S5). The MoS₂ devices with protected upper surface of the channel were fabricated in the similar process as discussed previously. But the exfoliation was done in the reverse way.

The devices were wire-bonded in ceramic leadless chip carrier obtained from Kyosera. The devices were heated till 120°C on a hotplate and immediately transferred into the low temperature cryostat. The cryostat was evacuated till 2×10^{-6} mbar pressure before starting experiments to reduce water vapour from the surface of the MoS₂ channel. All the measurements were carried out in same ultrahigh vacuum condition.

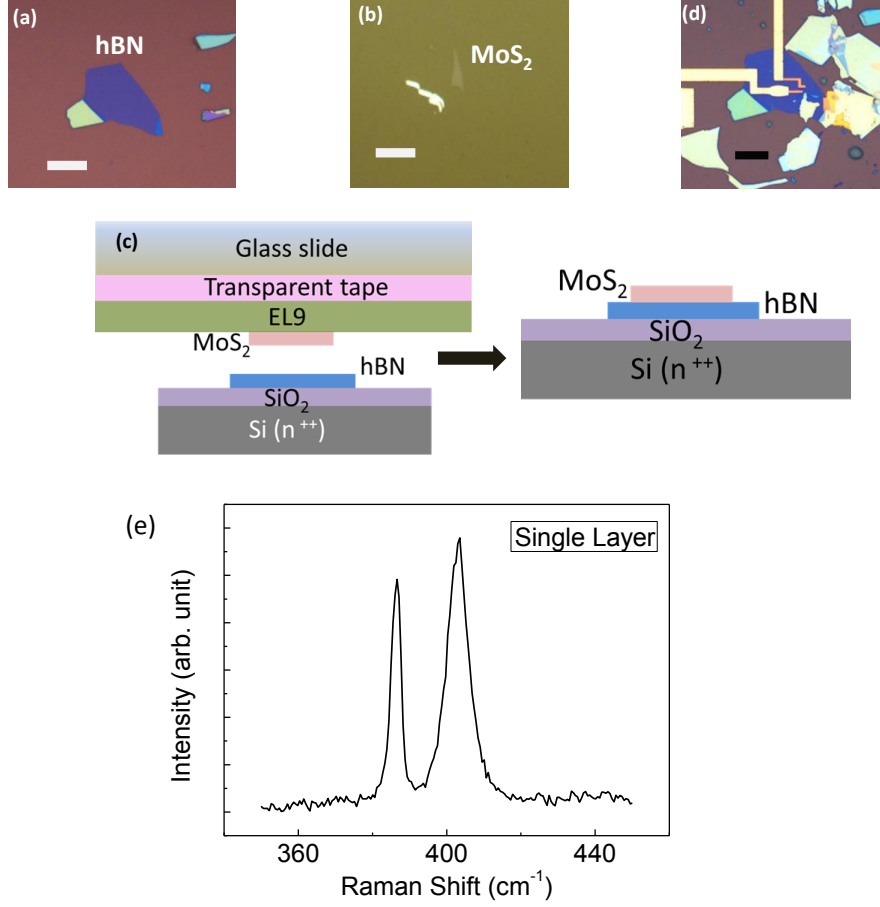


FIG. 6: (a) Thin layer of hBN on 275 nm of Si/SiO₂ substrate. (b) Single layer MoS₂ flake on glass-tape-EL9 stack. (c) Transfer of MoS₂ flake from polymer onto hBN. (d) Final MoS₂ on hBN device after liftoff. (e) Raman spectrum of a single layer MoS₂ film on Si/SiO₂ substrate after exfoliation.

B. Details of devices measured:

The detail of the devices are given in Table I.

C. Noise measurement Scheme:

For noise measurement the sample was biased with a constant ac voltage ~ 10 mV at 226 Hz from lockin. The sample current was passed through a low noise preamplifier and measured using lockin technique. The current fluctuation data as a function of time, called time series, was acquired with a high sampling rate data card. The time series data

TABLE I: Details of the devices:

Device	Layer Number	Device area (L×W) ^a	Mobility(μ_{FE}) ^b
1L-1	1	2×2.5	3
1L-2	1	5×8	9
1L-3	1	0.6×4.9	2.2
1L-4	1	1.1×4.9	2.8
1L-5	1	2.1×4.8	3.2
1L-6	1	2.7×1.6	0.7
1L-7	1	2×4	10
1L-8	1	0.16×1.9	0.5
1L-9	1	0.8×4	2.6
2L-1	2	2.8×2.5	22
2L-2	2	3×4.9	11
2L-3	2	1.9×2.2	10
1L-BN	1	3×4	4
2L-BN	2	0.8×1.8	3
4L-BN	4	1.7×2.7	20

^aboth dimensions in μm

^bin $\text{cm}^2/\text{V-s}$ near room temperature and $\Delta V_{BG} \sim 60\text{V}$

was Fourier transformed to obtain current noise power spectral density S_I/I^2 as a function of frequency $f^{48,49}$. The current power spectral density can be converted to conductivity fluctuation power spectral density S_σ/σ^2 using the relation

$$S_\sigma/\sigma^2 = S_I/I^2. \quad (2)$$

In the figures of the main manuscript and supplementary, we have plotted either “ S_σ/σ^2 at 1 Hz” or “integrated noise power $\langle\delta\sigma^2\rangle/\sigma^2$ ” as a measure of noise. $\langle\delta\sigma^2\rangle/\sigma^2$ is defined as the power spectral density integrated over the measurement frequency bandwidth i.e.

$$\langle\delta\sigma^2\rangle/\sigma^2 = \int_{f_1}^{f_2} S_\sigma/\sigma^2 df \quad (3)$$

where f_1 and f_2 are the lower and upper cut-off frequencies during the measurement.

The relation between $\frac{\langle \delta \sigma^2 \rangle}{\sigma^2}$ and $\frac{S_\sigma}{\sigma^2}$ at 1 Hz can be expressed as shown below:

$$\frac{\langle \delta \sigma^2 \rangle}{\sigma^2} = \int_{f_1}^{f_2} \frac{S_\sigma}{\sigma^2} df$$

and from Hooge relation, we have

$$\frac{S_\sigma}{\sigma^2} = \gamma_H / n A f^\alpha \quad (4)$$

Therefore, $|\frac{S_\sigma}{\sigma^2}|_{1 \text{ Hz}} = \gamma_H / n A$ and $\frac{S_\sigma}{\sigma^2} = \frac{|\frac{S_\sigma}{\sigma^2}|_{1 \text{ Hz}}}{f}$

For $1/f$ noise $\alpha \sim 1$ and hence

$$\begin{aligned} \frac{\langle \delta \sigma^2 \rangle}{\sigma^2} &= \int_{f_1}^{f_2} \frac{S_\sigma}{\sigma^2} df \\ &= \int_{f_1}^{f_2} \frac{|\frac{S_\sigma}{\sigma^2}|_{1 \text{ Hz}}}{f} df \\ &= |\frac{S_\sigma}{\sigma^2}|_{1 \text{ Hz}} \int_{f_1}^{f_2} df / f \\ &= |\frac{S_\sigma}{\sigma^2}|_{1 \text{ Hz}} \ln(f_2 / f_1) \end{aligned}$$

Therefore $\frac{\langle \delta \sigma^2 \rangle}{\sigma^2}$ and $|\frac{S_\sigma}{\sigma^2}|_{1 \text{ Hz}}$ are proportional to each other by a constant factor.

D. XPS measurement and data processing scheme:

The X-Ray Photoelectron Spectroscopy (XPS) measurements were performed on bulk MoS₂ with a commercial electron spectrometer from VSW Scientific instrument at a base pressure of 5×10^{-10} mbar. Mo 3*d* and S 2*p* core level spectra were recorded with Al K α radiation (photon energy 1486.6 eV) at a pass energy of 20 eV. The core level spectra were corrected for background using the Shirley algorithm, and chemically distinct species were resolved using nonlinear least-squares fitting procedure. A Lorentzian function representing the lifetime effect, convoluted with a Gaussian function representing the resolution was used to simulate the XPS peak shape. In order to minimize the number of free parameters in the decomposition process, we impose several constrains like, the same spin orbit splitting of various component feature of a particular core levels and the well-known branching ratios between the two spin-orbit split components.

E. XPS spectrum obtained from second time measurement:

We perform XPS measurements on two freshly cleaved samples. Results obtained from the first samples are shown in Fig. 1a and 1b of the main manuscript. The intense pair of peaks (blue solid line) at 229.6 eV and 232.8 eV binding energies (BE) with a separation of 3.2 eV, can be easily associated with the spin orbit split $3d_{5/2}$ and $3d_{3/2}$ pair of Mo^{4+} of 2H phase of MoS_2 ²¹. S 2p spectra in Fig 1b also has the main contribution from a spin orbit pair of the 2H phase of MoS_2 (blue solid line). In order to simulate the experimental spectra properly, we need to incorporate extra features (red solid line) in both S 2p and Mo 3d spectra. Relative intensities of these features, plotted in red in Figs 1a and 1b compare to the intensities of the features drawn in blue appear quite the same (5% relative intensity) in all figures, providing a consistency check from the independent analysis of Mo 3d and S 2p spectral features. Since the intensity of these extra species were very small compared to the main peaks, we performed the same XPS experiment in another freshly cleaved bulk crystal (see Fig. S2). The number of components and their relative intensity ratios are found to be the same for this sample as compared to the one reported in the main text. Additionally the small peak at higher BE side of the main Mo^{4+} feature in Mo 3d spectra probably coming from small amount of oxidized Mo^{6+} present in this sample as the BE of this feature matches well with what is reported in the literature for Mo^{6+} ions^{21,50,51}.

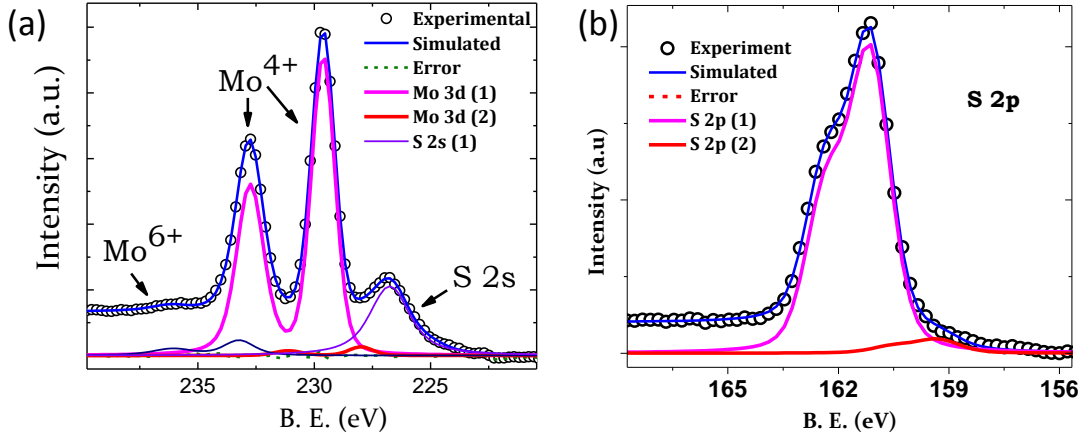


FIG. 7: XPS spectra of (a) Mo3d, S2s and (b) S2p taken from freshly cleaved bulk MoS_2 crystal at room temperature.

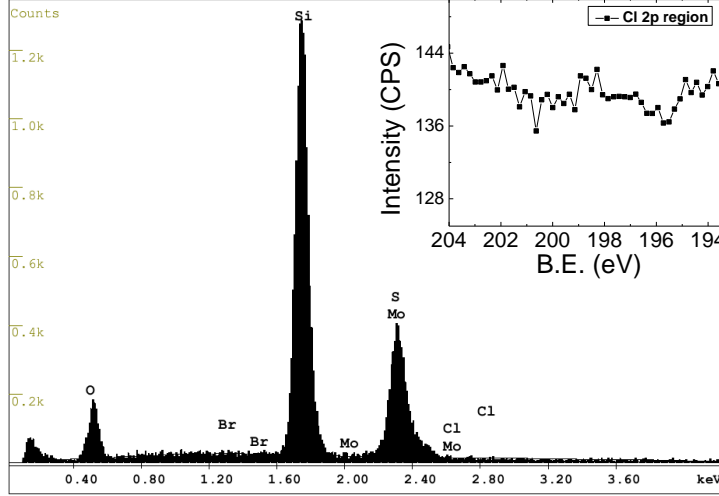


FIG. 8: EDX spectrum of bulk MoS₂ crystal taken at room temperature and high vacuum condition. Inset shows XPS scan of chlorine 2p region.

F. n-type doping in MoS₂ :

The origin of such n-doping is not very clear. Although, it was suggested that presence of halogen (Cl, Br) impurity in crystal may lead to n-type doping⁵, we couldn't find presence of halogen impurity in bulk natural crystal by EDX and XPS studies (see supplementary). Later on, it was also proposed that n-doping can possibly come from S vacancies in the crystal⁵² but a recent T dependent study reveals that this may not be the dominant cause³⁵.

We perform EDX and XPS study (see Fig. S3 and inset respectively) and find no presence of halogen impurity in naturally occurring MoS₂ crystal as discussed in Ref.⁵.

G. Localized to weak diffusive transition:

We believe that the localized electronic states in MoS₂ transistor become nearly extended with increasing carrier density (n) and T . This manifests as a localized to weak diffusive transition in the system as shown in Fig. S4(a). It is evident from the figure that transition temperature changes with carrier density as transfer characteristics at 200K and 300K intersects at $V_{BG}=54V$, whereas same for 240K, 260K and 300K intersects at $V_{BG}=30V$. Similar observations has been reported recently by two other groups^{34,35}. Here we mention that we didn't see this weak diffusive transition in every device till room temperature and V_{BG} as high as $\sim 70V$. We believe occurrence of such transition probably depends on intrinsic

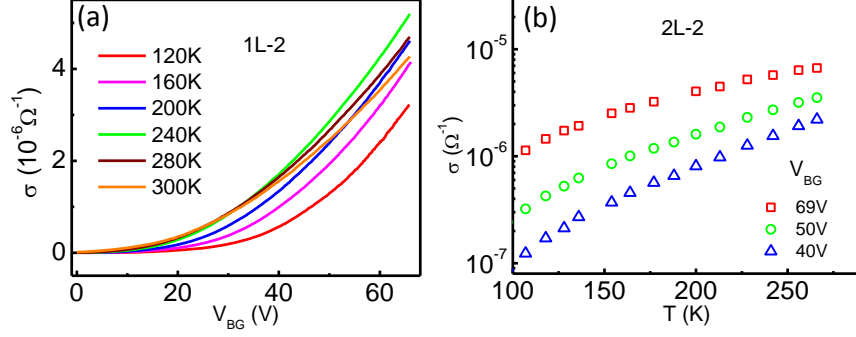


FIG. 9: (a) Backgate transfer characteristics of 1L-2 device showing localized to a weak diffusive transition at high T and V_{BG} . (b) σ as function of T at three different V_{BG} in a MoS₂ device with no localized to weak diffusive transition till room temperature.

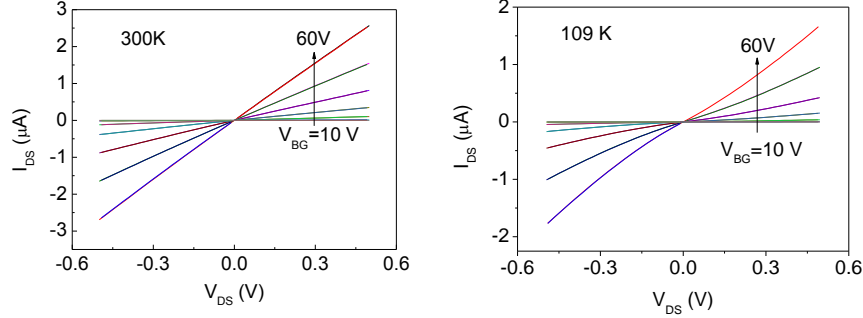


FIG. 10: Current-voltage characteristics of a typical single layer device at 300 K and 109 K at different backgate voltages.

disorder landscape of individual flake. There the σ vs. T will look like the unshaded region of Fig. 2c in the main text or as shown in Fig. S4(b).

H. Current-Voltage characteristics at 300K:

The typical current voltage relationship obtained in our devices near room temperature and low temperature are shown in Fig. S5. Such symmetric and linear current-voltage characteristics excludes dominance of Schottky barrier at the contacts.

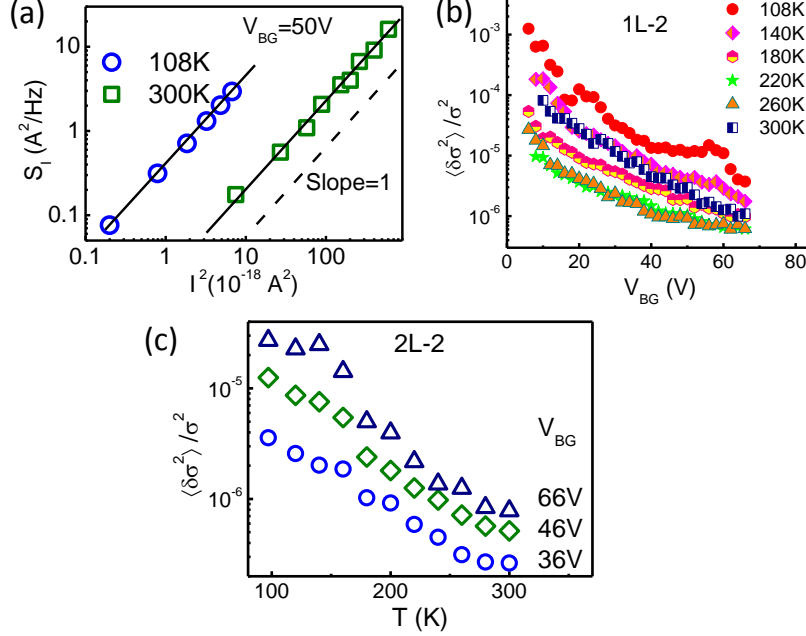


FIG. 11: (a) I^2 dependence of variance of noise S_I at high V_{BG} and low bias current showing a linear behavior both at high and low T . (b) Gate voltage dependence of normalized $1/f$ noise power integrated over the measurement bandwidth at various T for a single layer device. We found noise magnitude monotonically decrease as V_{BG} increases. (d) Normalized conductivity noise ($\langle \delta\sigma^2 \rangle / \sigma^2$) shows a monotonic decrease as T increases in a MoS₂ device with no localized to weak diffusive transition.

I. Noise measurement in ultrathin MoS₂ devices:

Before the noise measurement, all the devices were checked with I^2 dependence of variance of noise S_I at low bias current to avoid any heating induced effect (see Fig. S6a). The noise measurements were carried out at fixed T for different gate voltages along the transfer characteristic curve. We found that although the integrated noise power $\langle \delta\sigma^2 \rangle / \sigma^2$ monotonically decrease with increasing V_{BG} , the T dependence is non-monotonic as shown in Fig. S3b for device 1L-2. Such a non-monotonic T dependence also eliminate possibility of dominant contact noise in our devices. As we have already mentioned that all the devices have not shown such transition. In those cases noise monotonically decreases till room temperature as shown Fig. S6c.

J. Trap-channel tunnel model for pure number fluctuation:

For pure number fluctuation, the source-drain current noise can be written as^{25,26}

$$\frac{S_I}{I^2} = \left(\frac{g_m}{I^2} \right)^2 \frac{q^2 k_B T D_T}{W L C_{ox}^2 f \alpha} \quad (5)$$

where g_m is device transconductance, q is electronic charge, $k_B T$ is the thermal energy, D_T is trap density at channel-substrate interface per unit volume and energy, WL is active device area, C_{ox} is gate oxide capacitance per unit area, f is the frequency and α is the tunnelling attenuation coefficient of electronic wavefunction in $\text{SiO}_2 \sim 10^{10} \text{m}^{-1}$.

The noise measurement was performed at different V_{BG} with 2V interval along the transfer characteristic curve. Therefore, at a fixed gate voltage the current through the channel is constant. Then we can write equation S4 as

$$S_I = \frac{g_m^2 q^2 k_B T D_T}{W L C_{ox}^2 f \alpha}. \quad (6)$$

Using equation S5, We calculated $D_T \approx 6 \times 10^{19} - 7 \times 10^{20} \text{cm}^{-3} \text{eV}^{-1}$ in all our devices at room temperature. It has been already discussed in literature that due to contact resistance g_m is underestimated from transfer characteristic curve by 3-5 times^{3,53-55}. Therefore considering g_m^2 overestimates D_T by a factor of 10, the corrected value of $D_T \approx 6 \times 10^{18} - 7 \times 10^{19} \text{cm}^{-3} \text{eV}^{-1}$.

The surface trap charge density of SiO_2 is known to be $D_T \approx 5 \times 10^{17} \text{cm}^{-3} \text{eV}^{-1}$ near room temperature²⁵ which is one to two order less than the value obtained from our experiment.

K. Oscillatory conductance at low temperature:

We observed reproducible oscillations in conductivity due to resonant tunnelling between localized sites as shown in Fig. S7 (left)¹⁸. It was found that the peaks in oscillation shift as a function of both source-drain and gate bias as observed in quantum dot. A similar measurement is shown for device 1L-7 in Fig. S7 (right) at 18 K where we plot differential conductance dI/dV as a function of V_{DS} and V_{BG} . The shifting of conductance peaks in (V_{DS}, V_{BG}) plane is shown by the white lines which indicates two important consequences: First, the localized sites are not single particle localized states with large distribution of

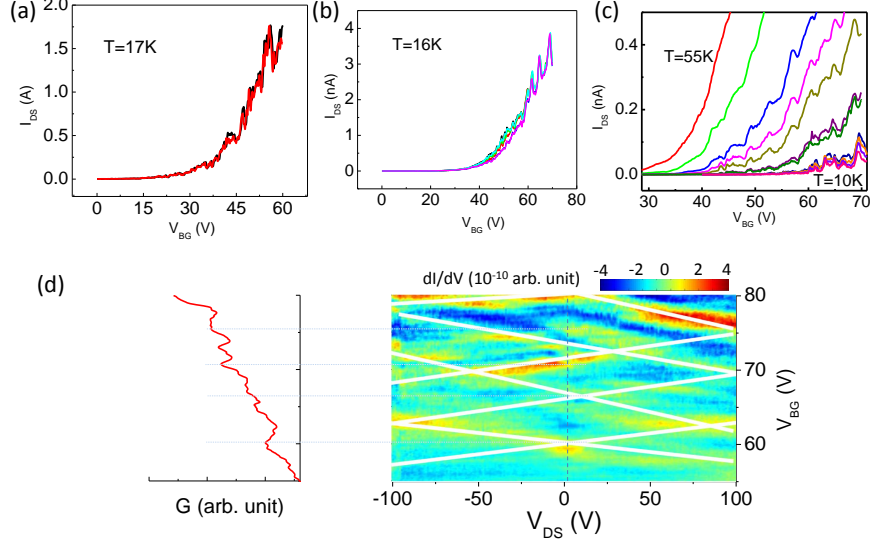


FIG. 12: (a)-(c) Reproducible oscillations in conductivity at low temperature for three different devices. (d) 2D map of differential conductance dI/dV as a function of V_{DS} and V_{BG} at $T = 18\text{ K}$. The white lines shows the evolution of the resonant tunnelling peaks in (V_{DS}, V_{BG}) plane (right). Oscillations along the dashed line (left).

charging energies, and second, approximate charging energy of the localized sites are $\sim 80 - 100\text{ meV}$.

L. calculation of ΔE for 1L-2 device:

This device also showed a weak diffusive transition but the T dependence was rather weak. Hence for this device we plot $\langle \delta\sigma^2 \rangle / \sigma^2$ as a function of $1/T$ which gives charging energy of $90 \pm 20\text{ meV}$, which is in close agreement with the value of ΔE , obtained from resonant tunnelling experiments. The number of data points are limited because we exclude the data beyond 300 K due to onset of hysteresis. In Fig. S8, the exponential fit yields, $\Delta E/k_B T \approx 1033 \Rightarrow \Delta E = 1033 k_B / e = 90\text{ meV}$.

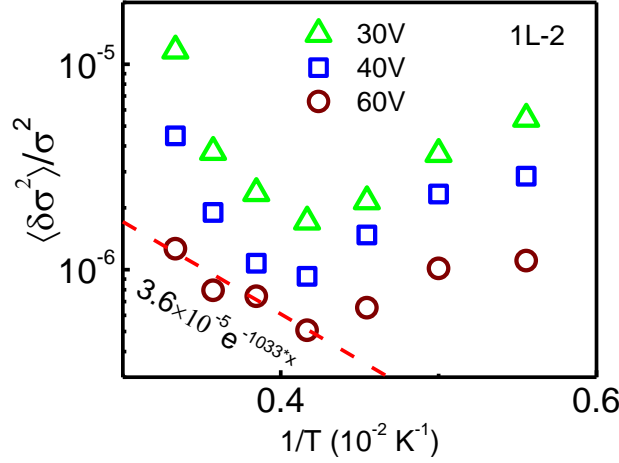


FIG. 13: (a) Normalised noise power $\langle \delta \sigma^2 \rangle / \sigma^2$ as a function of $1/T$.

M. Carrier density dependence of Hooge parameter (γ_H):

For $1/f$ noise, the Hooge relation can be written as $S_\sigma / \sigma^2 = \gamma_H / n A f$. In the diffusive regime, $S_\sigma / \sigma^2 \propto 1/n^2$ and $\sigma \propto n^2$ i.e. $\mu_{FE} \propto n$. Therefore, we have

$$\gamma_H \propto \frac{1}{\mu_{FE}} \quad (7)$$

N. Derivation of gate voltage and temperature dependence of noise:

At high T and V_{BG} , the localized states in 2H phase becomes nearly extended, and we assume $\sigma = ne\mu$ is valid. In this regime, we get

$$\frac{\delta \sigma}{\sigma} = \frac{\delta n}{n} + \frac{\delta \mu}{\mu} \quad (8)$$

where δn is the number of the carrier per unit area being exchanged between the semi-conducting 2H phase and electron-dense patches. $\delta \mu$ is the mobility fluctuation term. As number fluctuation is the dominant source of $1/f$ noise, we assume contribution from the second term is small compared to first term. Therefore we have

$$\frac{\delta \sigma}{\sigma} = \frac{\delta n}{n} \Rightarrow \frac{\langle \delta \sigma^2 \rangle}{\sigma^2} = \frac{\langle \delta n^2 \rangle}{n^2} = \frac{\langle \delta N^2 \rangle}{N^2} \quad (9)$$

where we have multiplied both the denominator and numerator by the area of 2H phase A_{2H} which is almost similar to total active device area A as 2H is the major phase in

MoS₂. N is the total number of the carriers in the 2H phase at a certain V_{BG} . $\langle \delta N^2 \rangle$ is the variance in total number of carriers fluctuating between the channel and the localized sites. The Fermi level E_F in the 2H phase will reach close to the mobility edge at high V_{BG} as shown in Fig. 4a (main manuscript). On the other hand, the nanometer-sized electron-dense regions will act as quantum dot and the highest filled and lowest empty energy levels will be Coulomb blockaded by the charging energy $\Delta E = e^2/C$, where C is the average capacitance of an localized region with respect to surroundings.

As the number fluctuation is happening predominantly between the channel and the electron-dense patches then $\langle \delta N^2 \rangle$ in 2H-channel will be related to $\langle \delta N_E^2 \rangle$ in the patches by the following equation

$$\langle \delta N^2 \rangle = N_E \langle \delta N_E^2 \rangle \quad (10)$$

where N_E is the total number of nanometer-sized electron-dense patches in the device area and $\langle \delta N_E^2 \rangle$ is the occupation fluctuation of a single electron-dense patch.

We will now focus on a single electron-dense patch. We define the probability that there will be no electron inside a patch as p_0 . Similarly, probability of one electron as p_1 and for n electrons as p_n . Therefore, we have

$$\begin{aligned} p_0 + p_1 + p_2 + p_3 + p_4 + \dots &= 1 \\ \Rightarrow p_0 + p_0 \exp\left[-\frac{\Delta E}{k_B T}\right] + p_0 \exp\left[-\frac{\Delta E + \Delta E_Q}{k_B T}\right] + p_0 \exp\left[-\frac{\Delta E + 2\Delta E_Q}{k_B T}\right] + \dots &= 1 \\ \Rightarrow p_0 \left\{ 1 + \exp\left[-\frac{\Delta E}{k_B T}\right] + \exp\left[-\frac{\Delta E + \Delta E_Q}{k_B T}\right] + \exp\left[-\frac{\Delta E + 2\Delta E_Q}{k_B T}\right] + \dots \right\} &= 1 \\ \Rightarrow p_0 \left\{ 1 + \exp\left[-\frac{\Delta E}{k_B T}\right] (1 + \exp\left[-\frac{\Delta E_Q}{k_B T}\right] + \exp\left[-\frac{2\Delta E_Q}{k_B T}\right] + \dots) \right\} &= 1 \\ \Rightarrow p_0 \left\{ 1 + \exp\left[-\frac{\Delta E}{k_B T}\right] \times \frac{1}{1 - \exp\left[-\frac{\Delta E_Q}{k_B T}\right]} \right\} &= 1 \\ \Rightarrow p_0 \left\{ 1 + \exp\left[-\frac{\Delta E}{k_B T}\right] \times \frac{1}{\epsilon} \right\} &= 1 \quad \text{where } \epsilon = 1 - \exp\left[-\frac{\Delta E_Q}{k_B T}\right] \\ \Rightarrow p_0 &= \frac{\epsilon}{\epsilon + \exp\left[-\frac{\Delta E}{k_B T}\right]} \end{aligned} \quad (11)$$

In order to evaluate $\langle \delta N^2 \rangle$ (equation S9), we first calculate $\langle \delta N_E^2 \rangle$ using

$$\langle \delta N_E^2 \rangle = \langle N_E^2 \rangle - \langle N_E \rangle^2 \quad (12)$$

The average occupation of a single electron-dense patch

$$\begin{aligned}
\langle N_E \rangle &= 0.p_0 + 1.p_1 + 2.p_2 + 3.p_3 + \dots \\
&= 0.p_0 + 1.p_0 \exp\left[-\frac{\Delta E}{k_B T}\right] + 2.p_0 \exp\left[-\frac{\Delta E + \Delta E_Q}{k_B T}\right] + 3.p_0 \exp\left[-\frac{\Delta E + 2\Delta E_Q}{k_B T}\right] + \dots \\
&= p_0 \exp\left[-\frac{\Delta E}{k_B T}\right] \left\{ 1. \exp\left[-0. \frac{\Delta E_Q}{k_B T}\right] + 2. \exp\left[-1. \frac{\Delta E_Q}{k_B T}\right] + 3. \exp\left[-2. \frac{\Delta E_Q}{k_B T}\right] + \dots \right\} \\
&= p_0 \exp\left[-\frac{\Delta E}{k_B T}\right] \times \frac{1}{(1 - \exp\left[-\frac{\Delta E_Q}{k_B T}\right])^2} \quad \left[\sum_{n=1}^{\infty} n x^{n-1} = \frac{1}{(1-x)^2} \right] \\
&= \frac{\epsilon \exp\left[-\frac{\Delta E}{k_B T}\right]}{\epsilon + \exp\left[-\frac{\Delta E}{k_B T}\right]} \times \frac{1}{\epsilon^2} \\
&= \frac{\exp\left[-\frac{\Delta E}{k_B T}\right]}{\epsilon(\epsilon + \exp\left[-\frac{\Delta E}{k_B T}\right])}
\end{aligned}$$

and

$$\begin{aligned}
\langle N_E^2 \rangle &= 0^2.p_0 + 1^2.p_1 + 2^2.p_2 + 3^2.p_3 + \dots \\
&= 1^2.p_0 \exp\left[-\frac{\Delta E}{k_B T}\right] + 2^2.p_0 \exp\left[-\frac{\Delta E + \Delta E_Q}{k_B T}\right] + 3^2.p_0 \exp\left[-\frac{\Delta E + 2\Delta E_Q}{k_B T}\right] + \dots \\
&= p_0 \exp\left[-\frac{\Delta E}{k_B T}\right] \left\{ 1^2. \exp\left[-0. \frac{\Delta E_Q}{k_B T}\right] + 2^2. \exp\left[-1. \frac{\Delta E_Q}{k_B T}\right] + 3^2. \exp\left[-2. \frac{\Delta E_Q}{k_B T}\right] + \dots \right\} \\
&= p_0 \exp\left[-\frac{\Delta E}{k_B T}\right] \times \frac{2 - \epsilon}{\epsilon^3} \quad \left[\sum_{n=1}^{\infty} n^2 x^{n-1} = \frac{1+x}{(1-x)^3} \right] \\
&= \frac{(2 - \epsilon) \exp\left[-\frac{\Delta E}{k_B T}\right]}{\epsilon^2(\epsilon + \exp\left[-\frac{\Delta E}{k_B T}\right])}
\end{aligned}$$

Therefore,

$$\begin{aligned}
\langle \delta N_E^2 \rangle &= \langle N_E^2 \rangle - \langle N_E \rangle^2 \\
&= \frac{(2 - \epsilon) \exp\left[-\frac{\Delta E}{k_B T}\right]}{\epsilon^2(\epsilon + \exp\left[-\frac{\Delta E}{k_B T}\right])} - \frac{\exp\left[-\frac{2\Delta E}{k_B T}\right]}{\epsilon^2(\epsilon + \exp\left[-\frac{\Delta E}{k_B T}\right])^2} \\
&= \frac{\exp\left[-\frac{\Delta E}{k_B T}\right]}{\epsilon^2} \times \left[\frac{2 - \epsilon}{\epsilon + \exp\left[-\frac{\Delta E}{k_B T}\right]} - \frac{\exp\left[-\frac{\Delta E}{k_B T}\right]}{(\epsilon + \exp\left[-\frac{\Delta E}{k_B T}\right])^2} \right] \\
&= \frac{\exp\left[-\frac{\Delta E}{k_B T}\right]}{\epsilon^2} \times \left[\frac{(2 - \epsilon)(\epsilon + \exp\left[-\frac{\Delta E}{k_B T}\right]) - \exp\left[-\frac{\Delta E}{k_B T}\right]}{(\epsilon + \exp\left[-\frac{\Delta E}{k_B T}\right])^2} \right] \\
&= \frac{\exp\left[-\frac{\Delta E}{k_B T}\right]}{\epsilon^2} \times \frac{2\epsilon + \exp\left[-\frac{\Delta E}{k_B T}\right] - \exp\left[-\frac{\Delta E}{k_B T}\right]}{(\epsilon + \exp\left[-\frac{\Delta E}{k_B T}\right])^2} \quad [\text{Assuming } \epsilon^2 \rightarrow 0 \text{ in the numerator}]
\end{aligned}$$

$$\begin{aligned}
&\approx \frac{\exp[-\frac{\Delta E}{k_B T}]}{\epsilon^2} \times \frac{2\epsilon}{\epsilon^2} \\
&= \frac{2 \exp[-\frac{\Delta E}{k_B T}]}{\epsilon^3}
\end{aligned}$$

where we assume $\epsilon > \exp[-\frac{\Delta E}{k_B T}]$, and this approximation is valid till the size of the patches are below 20 nm. We calculate

$$\begin{aligned}
\epsilon &= 1 - \exp[-\frac{\Delta E_Q}{k_B T}] \\
&\approx 1 - [1 - \frac{\Delta E_Q}{k_B T}] \quad [\Delta E_Q \ll k_B T \text{ for patch size more than 5 nm}] \\
&= \frac{\Delta E_Q}{k_B T}
\end{aligned}$$

Using Eq. S8, S9, and $\langle \delta N_E^2 \rangle$, we find

$$\begin{aligned}
\frac{\langle \delta \sigma^2 \rangle}{\sigma^2} &= \frac{\langle \delta N^2 \rangle}{N^2} \\
&= \frac{N_E}{N^2} \times \langle \delta N_E^2 \rangle \\
&= 2 \left[\frac{k_B T}{\Delta E_Q} \right]^3 \frac{N_E}{N^2} \exp[-\frac{\Delta E}{k_B T}]
\end{aligned}$$

As we have already shown that

$$\frac{\langle \delta \sigma^2 \rangle}{\sigma^2} = \left| \frac{S_\sigma}{\sigma^2} \right|_{1 \text{ Hz}} \ln(f_2/f_1) \quad (13)$$

Therefore, we obtain

$$\left| \frac{S_\sigma}{\sigma^2} \right|_{1 \text{ Hz}} = \frac{2}{\ln(f_2/f_1)} \left[\frac{k_B T}{\Delta E_Q} \right]^3 \frac{N_E}{N^2} \exp[-\frac{\Delta E}{k_B T}] \quad (14)$$

O. Calculation of Hooke parameter (γ_H) from equation 1 in main text:

$$\frac{\langle \delta \sigma^2 \rangle}{\sigma^2} = 2 \left[\frac{k_B T}{\Delta E_Q} \right]^3 \frac{N_E}{N^2} \exp[-\frac{\Delta E}{k_B T}] \quad (15)$$

$$\begin{aligned}
\frac{\langle \delta \sigma^2 \rangle}{\sigma^2} &= \int_{f_1}^{f_2} S_\sigma / \sigma^2 df \quad [f_1 \text{ and } f_2 \text{ represent measured frequency bandwidth}] \\
&= \frac{\gamma_H}{N} \int_{f_1}^{f_2} df / f \quad [\text{where we use the Hooge relation } S_\sigma / \sigma^2 = \gamma_H \frac{1}{Nf}] \\
&= \frac{\gamma_H}{N} \ln(f_2 / f_1)
\end{aligned}$$

Therefore,

$$\gamma_H = \frac{2}{\ln(f_2/f_1)} \left[\frac{k_B T}{\Delta E_Q} \right]^3 \frac{N_E}{N} \exp\left[-\frac{\Delta E}{k_B T}\right] \quad (16)$$

This equation predicts $\gamma_H \propto 1/n$. As $\sigma \propto n^2$ at high temperature and gate voltages, the field effect mobility $\mu_{FE} \propto n$. Therefore, equation S9 suggests that the Hooge parameter is inversely proportional to μ_{FE} .

If A and t are the area and thickness respectively of the MoS₂ channel then

$$N_E = N_p \times At = \frac{0.05}{D^2 t} At = \frac{0.05A}{D^2} \quad (17)$$

We calculate $\Delta E_Q \simeq \frac{h^2}{8m^* D^2} \simeq 1.6$ meV assuming m^* to be roughly equal to free electron mass. Using $f_1 = 0.03$, $f_2 = 6.8$ Hz and $k_B T = 26$ meV, we obtain $\gamma_H \approx 0.2$ at carrier density $n = 4.5 \times 10^{12} \text{cm}^{-2}$.

-
- ¹ B. Radisavljevic, A. Radenovic, J. Brivio, V. Giacometti, and A. Kis, Nat. Nano. **6**, 147 (2011).
 - ² H. Liu, A. T. Neal, and P. D. Ye, ACS Nano **6**, 8563 (2012).
 - ³ B. Radisavljevic, M. B. Whitwick, and A. Kis, ACS Nano **5**, 9934 (2011).
 - ⁴ H. Wang, L. Yu, Y.-H. Lee, Y. Shi, A. Hsu, M. L. Chin, L.-J. Li, M. Dubey, J. Kong, and T. Palacios, Nano Letters **12**, 4674 (2012).
 - ⁵ Z. Yin, H. Li, H. Li, L. Jiang, Y. Shi, Y. Sun, G. Lu, Q. Zhang, X. Chen, and H. Zhang, ACS Nano **6**, 74 (2012).
 - ⁶ K. Roy, M. Padmanabhan, S. Goswami, T. Phanindra Sai, G. Ramalingam, S. Raghavan, and A. Ghosh, Nat Nano **8**, 826 (2013).
 - ⁷ K. Roy, M. Padmanabhan, S. Goswami, T. P. Sai, S. Kaushal, and A. Ghosh, Solid State Communications **175-176**, 35 (2013).
 - ⁸ Y. Yoon, K. Ganapathi, and S. Salahuddin, Nano Letters **11**, 3768 (2011).
 - ⁹ K. Kaasbjerg, K. S. Thygesen, and K. W. Jacobsen, Phys. Rev. B **85**, 115317 (2012).

- ¹⁰ S. Das, H.-Y. Chen, A. V. Penumatcha, and J. Appenzeller, Nano Letters **13**, 100 (2013).
- ¹¹ H. Liu and P. Ye, Electron Device Letters, IEEE **33**, 546 (2012).
- ¹² D. J. Late, B. Liu, H. S. S. R. Matte, V. P. Dravid, and C. N. R. Rao, ACS Nano **6**, 5635 (2012).
- ¹³ M. Katsnelson and A. Geim, Phil. Trans. R. Soc. A **366**, 195 (2008).
- ¹⁴ S. Adam, E. Hwang, E. Rossi, and S. D. Sarma, Solid State Communications **149**, 1072 (2009).
- ¹⁵ J.-H. Chen, C. Jang, S. Adam, M. S. Fuhrer, E. D. Williams, and M. Ishigami, Nat. Phys. **4**, 377 (2008).
- ¹⁶ A. N. Pal, S. Ghatak, V. Kochat, E. S. Sneha, A. Sampathkumar, S. Raghavan, and A. Ghosh, ACS Nano **5**, 2075 (2011).
- ¹⁷ A. Ayari, E. Cobas, O. Ogundadegbe, and M. S. Fuhrer, Journal of Applied Physics **101**, 014507 (2007).
- ¹⁸ S. Ghatak, A. N. Pal, and A. Ghosh, ACS Nano **5**, 7707 (2011).
- ¹⁹ H. Qiu, T. Xu, Z. Wang, W. Ren, H. Nan, Z. Ni, Q. Chen, S. Yuan, F. Miao, F. Song, et al., Nat Commun **4**, 2642 (2013).
- ²⁰ B. Windom, W. Sawyer, and D. Hahn, Tribology Letters **42**, 301 (2011).
- ²¹ G. Eda, H. Yamaguchi, D. Voiry, T. Fujita, M. Chen, and M. Chhowalla, Nano Letters **11**, 5111 (2011).
- ²² U. Chandni, A. Ghosh, H. S. Vijaya, and S. Mohan, Phys. Rev. Lett. **102**, 025701 (2009).
- ²³ A. N. Pal and A. Ghosh, Applied Physics Letters **95**, 082105 (2009).
- ²⁴ A. N. Pal and A. Ghosh, Phys. Rev. Lett. **102**, 126805 (2009).
- ²⁵ R. Jayaraman and C. G. Sodini, IEEE Trans. Electron Device **36**, 1773 (1989).
- ²⁶ E. G. Ioannidis, A. Tsormpatzoglou, D. H. Tassis, C. A. Dimitriadis, F. Templier, and G. Kamarinos, J. Appl. Phys. **108**, 106103 (2000).
- ²⁷ S. Adam and S. Das Sarma, Phys. Rev. B **77**, 115436 (2008).
- ²⁸ S. Berleb, A. G. Muckl, W. Brutting, and M. Schwoerer, Synthetic Metals **111-112**, 341 (2000).
- ²⁹ R. W. I. de Boer, M. E. Gershenson, A. F. Morpurgo, and V. Podzorov, physica status solidi (a) **201**, 1302 (2004).
- ³⁰ D. Joung, A. Chunder, L. Zhai, and S. I. Khondaker, Applied Physics Letters **97**, 093105 (2010).
- ³¹ S. Ghatak and A. Ghosh, Applied Physics Letters **103**, 122103 (2013).
- ³² V. Kumar, S. C. Jain, A. K. Kapoor, J. Poortmans, and R. Mertens, Journal of Applied Physics

- 94**, 1283 (2003).
- ³³ B. I. Shklovskii, Phys. Rev. B **67**, 045201 (2003).
- ³⁴ B. Radisavljevic and A. Kis, Nat Mater **12**, 815 (2013).
- ³⁵ B. Baugher, H. O. H. Churchill, Y. Yang, and P. Jarillo-Herrero, Nano Letters **13**, 4212 (2013).
- ³⁶ P. Dutta and P. M. Horn, Rev. Mod. Phys. **53**, 497 (1981).
- ³⁷ A. L. McWhorter, *Semiconductor Surface Physics* (Philadelphia, University of Pennsylvania Press, 1957).
- ³⁸ Y. Zhang, E. E. Mendez, and X. Du, ACS Nano **5**, 8124 (2011).
- ³⁹ J. Renteria, R. Samnakay, S. L. Rumyantsev, P. Goli, M. S. Shur, and A. A. Balandin, arXiv.org e-Print archive **arXiv:1312.6868** (2013).
- ⁴⁰ C. R. Dean, A. F. Young, I. Meric, C. Lee, L. Wang, S. Sorgenfrei, K. Watanabe, T. Taniguchi, P. Kim, K. L. Shepard, et al., Nat. Nano. **5**, 722 (2010).
- ⁴¹ Y. Wang, X. Luo, N. Zhang, M. R. Laskar, L. Ma, Y. Wu, S. Rajan, and W. Lu, arXiv.org e-Print archive **1310.6484** (2013).
- ⁴² V. K. Sangwan, H. N. Arnold, D. Jariwala, T. J. Marks, L. J. Lauhon, and M. C. Hersam, Nano Letters **13**, 4351 (2013).
- ⁴³ S. McDonnell, R. Addou, C. Buie, R. M. Wallace, and C. L. Hinkle, ACS Nano **doi:10.1021/nn500044q**, null (0).
- ⁴⁴ M. M. Benameur, B. Radisavljevic, J. S. Hron, S. Sahoo, H. Berger, and A. Kis, Nanotechnology **22**, 125706 (2011).
- ⁴⁵ A. Castellanos-Gomez, N. Agrait, and G. Rubio-Bollinger, Applied Physics Letters **96**, 213116 (2010).
- ⁴⁶ C. Lee, H. Yan, L. E. Brus, T. F. Heinz, J. Hone, and S. Ryu, ACS Nano **4**, 2695 (2010).
- ⁴⁷ P. J. Zomer, S. P. Dash, N. Tombros, and B. J. van Wees, Applied Physics Letters **99**, 232104 (2011).
- ⁴⁸ J. H. Scofield, Review of Scientific Instruments **58**, 985 (1987).
- ⁴⁹ A. Ghosh, S. Kar, A. Bid, and A. K. Raychaudhuri, arXiv.org e-Print archive **arXiv:cond-mat/0402130** (2008).
- ⁵⁰ D. D. Sarma, P. Mahadevan, T. Saha-Dasgupta, S. Ray, and A. Kumar, Phys. Rev. Lett. **85**, 2549 (2000).
- ⁵¹ D. D. Sarma and C. N. R. Rao, Journal of Electron Spectroscopy and Related Phenomena **20**,

25 (1980).

⁵² J. T. Ye, Y. J. Zhang, R. Akashi, M. S. Bahramy, R. Arita, and Y. Iwasa, *Science* **338**, 1193 (2012).

⁵³ N. R. Pradhan, D. Rhodes, Q. Zhang, S. Talapatra, M. Terrones, P. M. Ajayan, and L. Balicas, *Applied Physics Letters* **102**, 123105 (2013).

⁵⁴ M. S. Fuhrer and J. Hone, *Nat Nano* **8**, 146 (2013).

⁵⁵ B. Radisavljevic and A. Kis, *Nat Nano* **8**, 147 (2013).